IEEE Robotics and Automation Letters (RAL) paper presented at
2024 IEEE/RSJ International Conference on Intelligent Robots and Systems (IROS)
October 14-18, 2024. Abu Dhabi, UAE

Swift: Transition Characterization and Motion Analysis of a Multimodal Underwater Vehicle

Hexiong Zhou, Junjun Cao, Jian Fu, Zheng Zeng, Baoheng Yao, Zhihua Mao, Lian Lian

***Abstract*—This letter proposes a novel conceptual multimodal underwater vehicle, named "Swift", which is capable of dexterous attitude transition for multiple operation modes. Aside from being competent to adjust pitch and roll angles in the range of -90° to 90°, it can achieve in-situ heading angle maneuvering adjustment with nearly 150° in cramped space, without any assistance of external driving mechanisms such as propeller or rudder. Ingenious configuration, design principles, and maneuvering control sequences of actuators are proposed for innovative attitude transition. Other characteristics, such as the shape and internal drive structures, are identical to classic underwater gliders without further upgrading, which offers great portability and extensibility. The description of the transient behavior during agile attitude transitions, particularly the effective estimation of in-situ heading angle adjustment, is greatly facilitated by transition dynamics with modified hydrodynamic compositions. The consistent results of dynamics simulation and various experiments demonstrate the performance of multi-mode locomotion and promote the transition characterization of the prototype.**

***Index Terms*—Multimodal underwater vehicle, mode transition, dexterous attitude adjustment, multimodal control.**

I. INTRODUCTION

IN the past decade, more in-situ observation data have been collected by traditional unmanned marine robots, such as autonomous underwater vehicle (AUV), underwater glider (UG), and (moored or drifting) Buoy, than was collected throughout the entire 20th century, which has made enormous contribution to marine scientific research [1]. The in-depth understanding of the ocean mechanism has brought new requirements and considerable challenges to obtain long-term continuous, multidisciplinary, three-dimensional in-situ observation data [2], and promoted the development of multimodal unmanned vehicle technology [3].

Multimodal underwater vehicle refers to the harmonious integration of at least two operating features or driving mechanisms on one vehicle. The compatibility and switchability of multi-modes are the key technologies in the development of multimodal platform. In our previous work, we proposed a new concept of multimodal underwater vehicle (MUV), which is compatible with multiple operating patterns of Argo float, UG and AUV, and is qualified for multi-scale comprehensive high-resolution observation [4]. The premise of realizing the compatibility between Argo mode and UG mode is the transition between horizontal and vertical attitude. However, there are still limitations to the present underwater vehicle technology's dexterity and practicable range of attitude transition.

The attitude adjustment ability directly impacts the maneuverability of the underwater vehicle. Classic UG reconfigures the location of the center of gravity (CG) by driving the internal actuation, to achieve pitch and roll regulation, and the heading is modified by the hydrodynamic moment induced by the roll angle during the gliding process. The conventional driving mechanism, however, is typically accompanied by turning radii of several dozen meters and can only accomplish a limited viable attitude adjustment scope. The turning radius of Seaglider is close to 30 meters [5]. The ROUGHIE is specially designed for high-performance manoeuvring with a maximum roll angle of +/-60 degree, but still has a minimum turning radius of 3m when adjusting the heading [6]. Obviously, the classic UG has historically not been incompetent for making in-situ heading adjustment [7]. It is challenging to quickly change the heading angle for typical congested areas like coastal water or polar ice crevasses. More tight turns can be achieved by the external actuation with rudder surface or bionic caudal fin swing [8], [9]. The vector arrangement of the thrusters on an AUV or ROV may change the heading angle in real time, but in order to significantly change the pitch or roll angle, the vehicle is often in motion [10]–[12]. Additionally, adding more thrusters results in a significant strain on energy usage in addition to reducing economy. A hybrid underwater hexapod robot from NWPU based on C-shape leg and righting moment can climb a 90 degrees wall, but it does not invest in improving the roll adjustment capacity [13]. With a minimum turning radius of 30 meters, the Smart Argo from SJTU can modify the pitching attitude of +60/-85 degrees [14]. A hybrid underwater profiler proposed by ZJU has a feasible pitch adjustment scope of +90/0 degrees, with a turning radius of several meters [15]. The Petrel-X-PLUS [16] aims to utilise two independent rotating mechanisms to achieve a pitching adjustment ranging from plus to minus 90°. Through sea trials, it has been proved that this enhanced pitch adjustment capacity effectively enhances the vehicle's station-keeping performance. Nevertheless, the vehicle has yet to overcome the persistent issue of sluggish heading adjustment found in conventional underwater gliders, which results in a turning radius of dozens of metres. Furthermore, the analysis of the vehicle's dynamics mostly emphasised the terminal state of the vertical pitching attitude, while overlooking the depiction of the ongoing transient behaviour during the attitude transition phase. Detailed performance characterization about attitude adjustment and parameters of diverse underwater vehicles are

---

This work is supported by China Postdoctoral Science Foundation(2023M732196, 2023TQ0214, GZC20231551), Oceanic Interdisciplinary Program of Shanghai Jiao Tong University under Grant SL2022ZD206, National Key R&D Program of China (2021YFC2801600), and Natural Science Foundation of China under grant number 42206189.(Corresponding author: Baoheng Yao)

The authors are with the School of Oceanography, Shanghai Jiao Tong University, Shanghai, China(e-mail:zhou_hexiong@sjtu.edu.cn)

TABLE I
COMPARISON OF ATTITUDE REGULATION PERFORMANCE OF VARIOUS UNDERWATER VEHICLES.

Prototype	Slocum [17]	HUP-ZJU [15]	Smart Argo [14]	ROUGHIE [6]	HUHR-NWPU [13]	Grace [9]	Petrel-X-Plus [16]	Swift
Mass	52kg	82kg	200kg	12.8kg	No data	9kg	230kg	50kg
Pitch adjustment performance	+60/-60 degrees	+90/0 degrees	+50/-90 degrees	No data	+90/0 degrees	+60/-60 degrees	+90/-90 degrees	+90/-90 degrees
Roll adjustment performance	No data	No data	+90/-90 degrees	+/-60 degrees	0 degree	+30/-30 degrees	No data	+90/-90 degrees
Heading adjustment performance	Turning radius 7m by internal actuation	Turning radius dozens of meters by internal actuation	Turning radius 30m by internal actuation	Turning radius 3m by internal actuation	In-situ adjustment by external thruster vector allocation	Turning radius 1m by fish-like tail	Turning radius dozens of meters by internal actuation	In-situ adjustment of 150°by internal actuation

shown in Table I.

This letter reports a novel multimodal underwater vehicle with dexterous attitude transition capacity, named Swift. The vehicle is interoperable with various operation modes for ocean multi-scale observation tasks. The main contributions include, (1) ingenious fabrication configuration, design criteria, and maneuvering control sequences permit a large-scale attitude feasible region, particularly for a significant range of in-situ heading adjustment; (2) transition dynamics with the modified hydrodynamic compositions facilitate the description of the transient behavior between agile attitude transitions, with an error of merely 8 degrees from experimental results in estimating the in-situ heading angle adjustment. The results of pool-based experiments for transition performance assessment are in good agreement with the simulated results. Details refer to the video attachment.

II. PROTOTYPE VEHICLE FABRICATION

Swift consists primarily of a buoyancy regulating system (BRS), an attitude regulating system (ARS), and an electrical system, with a gross weight of 50kg, a primary body length of 1800mm and 200mm-outer-diameter. The geometries and details of the estimated parameters of Swift are given in Table II. Fig. 1(a) exhibits its exterior details. Fast-assembling design enables the independent sections of each subsystem to be quickly spliced through connector. Swift's skillful handling of significant attitude adjustment range is made possible by its thoughtfully designed ARS and BRS.

Fig. 2 exhibits the interior details of the ARS. The movable mass (MM), which consists of two 6S power lithium batteries, aluminum alloy mounting plates and screws, weighs 3.2 kg in total, is designed to combine translation and rotation action to maximize the use of limited available area. The effective travel of the translational part of MM is 100mm, and the rotatable part can be rotated globally. As described in our previous work [4], the weight of the rotatable part needs meticulous configuration. When the following torque balance relationship between the movable mass m_p (eccentric distance R_p) and the static mass m_s (eccentric distance Z_{rs}) is satisfied,

$$m_p R_p - m_s Z_{rs} = 0. \tag{1}$$

TABLE II
GEOMETRIES AND ESTIMATED MODEL PARAMETERS OF SWIFT.

Geometries & hydrodynamic coefficients	Value
Static block m_s	41.19kg
Movable block m_p	8.81kg
Net buoyancy m_0	$m_0 \in [-0.5, 0.5]$kg
Displaced fluid mass	50kg
Position of the movable block $\boldsymbol{r}_p$	$R_p = 0.045$m, $\gamma \in [-\pi, \pi]$ $r_{p1} \in [0.3516, 0.4516]$m
Total length of the vehicle L_h	1.84 m
Cross-sectional area of the hull S	$0.06m^2$
Coefficients of drag force	$K_{D0} = 7.19$, $K_D = 386.29$
Coefficients of lift force	$K_{L0} = 0$, $K_L = 440.99$
Coefficients of side force	$K_\beta = -115.65$
Coefficients of roll moment	$K_{MR} = -58.27$, $K_p = -19.83$ $K'_p = -0.21$
Coefficients of pitch moment	$K_{M0} = 0$, $K_M = -65.84$ $K_q = -205.64$,$K'_q = -2.03$
Coefficients of yaw moment	$K_{MY} = 0$ $K_r = -205.64$,$K'_r = -17.51$
Duct diameter D_p	0.15m
Coefficients of the propeller	$C_F = 0.21$, $C_T = 0.033$
Coefficients of the rudder	$Y_{\delta v} = 0.21$, $N_{\delta v} = 0.21$ $K_{\delta v} = 0$
Model parameters of the actuators	$\Upsilon_1 = 1.54$, $\Upsilon_2 = 1.16$, $\Upsilon_3 = 3.47$ $\kappa_1 = 5.6e-3$, $\kappa_2 = 2.7e-3$ $\kappa_3 = 6.5e-3$

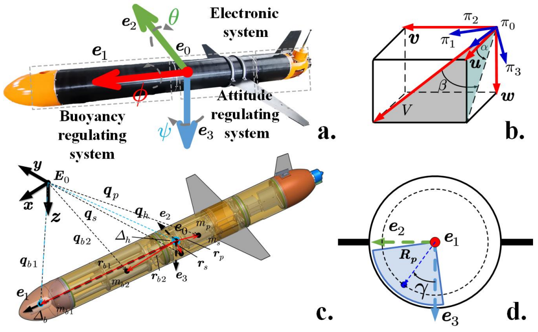

Fig. 1. Configuration and coordinate system definition. **A**. Configuration of Swift with the marks on the body coordinate system. **B**. Velocity-referenced frame. **C**. Mass distribution of Swift in the body-fixed reference frame and inertia reference frame. **D**. Schematic diagram of axial cross-section.

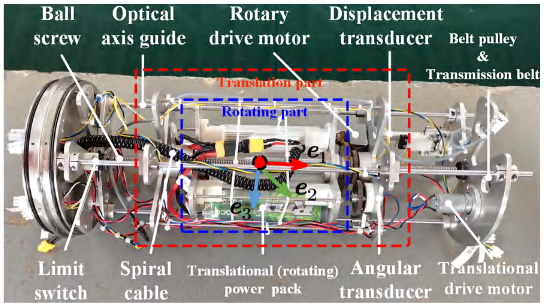

Fig. 2. Interior photograph of ARS showing the translation and rotation mechanism.

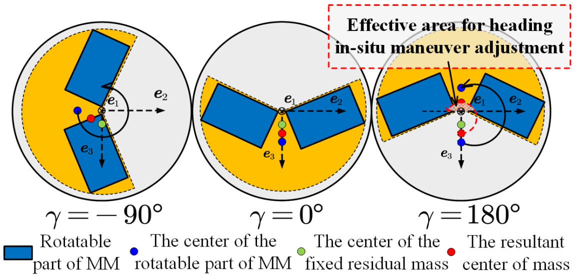

Fig. 3. Sketch of cross-section of the rotatable mass of MM around the central axis viewing from the stern.

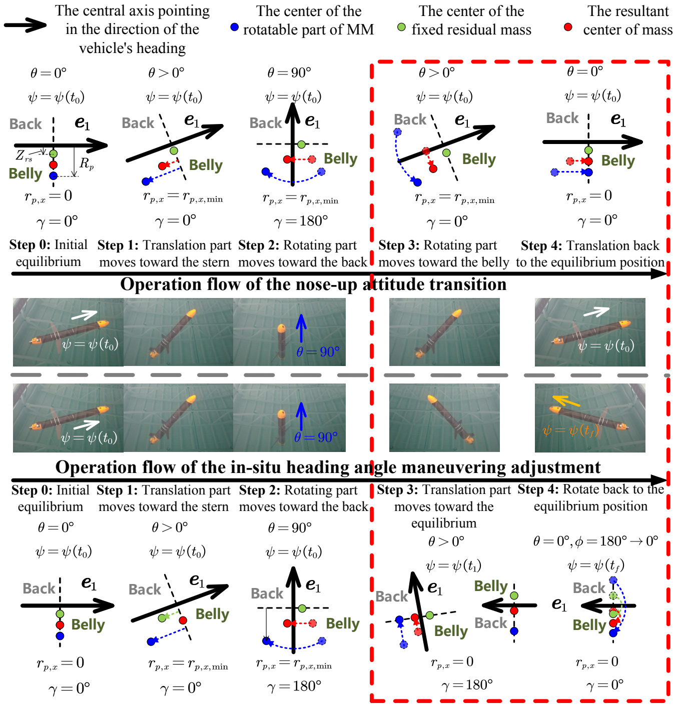

Fig. 4. Operation flow of the nose-up attitude transition and in-situ heading angle maneuvering execution (Sketch of the longitudinal section of the vehicle viewed from the right wing).

after the rotatable part is rotated to the top with the rotation angle $\gamma = 180°$ around the central axis of the system $\boldsymbol{e}_0\boldsymbol{e}_1$, the resultant center of gravity (CG) will be reconfigured to $\boldsymbol{e}_0\boldsymbol{e}_1$. Considering that the roll angle ϕ in the stable suspension state has the following relationship with the rotation angle of MM,

$$m_p R_p \sin(\gamma + \phi) + m_s Z_{rs} \sin\phi = 0. \tag{2}$$

then the relationship $\phi = -\frac{\gamma}{2}$ can be yielded.

In contrast to the prior version, a novel design principle is proposed to realize the in-situ heading adjustment, which highlights that the moment of the rotatable part of the relation (1) should be slightly larger than the other one, as shown in Fig. 3. It enables the moving trajectory of the resultant CG to be extended to the top of the $\boldsymbol{e}_0 - \boldsymbol{e}_1\boldsymbol{e}_2$ plane along the opposite direction of the $\boldsymbol{e}_0\boldsymbol{e}_3$ axis. The rotatable part of the mass can be arranged near the central axis without moving to the top. When the rotatable part of MM moves in the belly area of the vehicle (below the plane $\boldsymbol{e}_0 - \boldsymbol{e}_1\boldsymbol{e}_2$), the operating mode is the same as that of the traditional UG. When moving to the plane $\boldsymbol{e}_0 - \boldsymbol{e}_1\boldsymbol{e}_2$, the vertical attitude transition can be realized by collaboratively regulating the translation part. Another distinctive design of actuator control sequences (as illustrated in Fig. 4) is proposed to realize in-situ heading angle maneuvering adjustment, only by ingenious exchanging the control sequences of actuators in Step 3 and Step 4 (control sequence for translating or rotating MM), which can be regarded as an upgrade in the ability to regulate pitching attitude drastically. In the operation flow of in-situ heading adjustment, Step 3 is set to prioritize the translation of the MM to the equilibrium, and the rotation of the MM is set as a subsequent operation (Step 4). After Step 3, Swift exhibits an unusual posture with the belly facing upward, due to a significantly reduced metacentric height and a resultant center of gravity that has been elevated to the back direction. After Step 4, the lower right corner of Fig. 4 illustrates the spontaneous maneuver wherein the vehicle transitions from a belly-up position to a back-up orientation. For more details, see experimental results in Section 4.B and the attached animation.

The BRS is elaborately designed to adjust the floating condition of the vehicle while promoting the high metacentricity. The BRS simultaneously adjusts the position of four pistons through the linear actuator to adjust the amount of oil in the external bladder in real time. With a combined weight of 3.46kg, the primary drive spindle, four piston rods, and mounting disk are all moveable elements and nearly twice as heavy as the lithium battery pack. The reciprocation of the linear actuator leads to the migration of the CG position along the axis $\boldsymbol{e}_0\boldsymbol{e}_1$. It is specially designed to configure the movable part of BRS towards the bow of the vehicle, as shown in Fig. 5. During the diving (floating) motion, the elongated (shortened) linear actuator enables the oil to flow inward (outward), the buoyancy is reduced (increased) and the posture is bowed (risen), and the resultant CG moves toward the positive (negative) direction of the axis $\boldsymbol{e}_0\boldsymbol{e}_1$. Obviously, when the heading orientation is consistent with the motion direction, the auxiliary adjustment of metacentric height h_{BC} by BRS is extremely efficient in enhancing the verticality of the vertical pitching attitude. The reconciliated manipulation of ARS and BRS is the key to realizing dexterous attitude transition, referring to the subsequent experimental description.

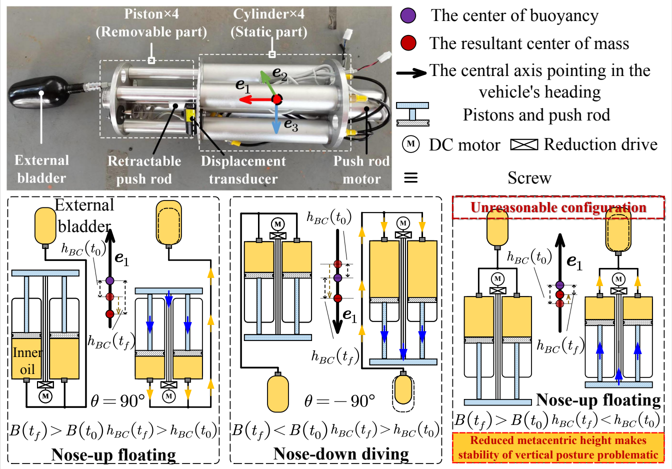

Fig. 5. Interior photograph and schematic diagram of BRS showing buoyancy and attitude coupling regulation.

III. TRANSITION DYNAMICS

Three frames and the mass distribution of Swift are defined in Fig. 1: the inertia reference frame (IRF) $\{\boldsymbol{E}_0 - \boldsymbol{xyz}\}$, whose plane $\{\boldsymbol{E}_0\boldsymbol{xy}\}$ is fixed on the water surface, the body-fixed reference frame (BRF) $\{\boldsymbol{e}_0 - \boldsymbol{e}_1\boldsymbol{e}_2\boldsymbol{e}_3\}$, and the velocity-referenced frame (VRF)$\{\boldsymbol{\pi}_0 - \boldsymbol{\pi}_1\boldsymbol{\pi}_2\boldsymbol{\pi}_3\}$. Define Hamilton form-based unit quaternion $\boldsymbol{Q} = \left[q_0, \boldsymbol{q}_v^T\right]^T$, where q_0 and $\boldsymbol{q}_v = [q_1, q_2, q_3]^T$ represent the scalar and vector parts of the quaternion respectively. The generalized position vector in IRF is defined as $\boldsymbol{\eta} = \left[\boldsymbol{b}^T, \boldsymbol{Q}^T\right]^T$, with the position vector $\boldsymbol{b} = [x, y, z]^T$. The generalized motion state vector in BRF is defined as $\boldsymbol{\varLambda} = \left[\boldsymbol{V}^T, \boldsymbol{\varOmega}^T\right]^T$. The Euler angle is $\boldsymbol{\theta} = [\phi, \theta, \psi]^T$. The linear and angular velocity vectors in BRF are $\boldsymbol{V} = [u, v, w]^T$ and $\boldsymbol{\varOmega} = [p, q, r]^T$ respectively. The kinematic equation represented by the quaternion can be expressed as,

$$\dot{\boldsymbol{\eta}} = \boldsymbol{J}\left(\boldsymbol{\eta}, \boldsymbol{\varOmega}\right)\boldsymbol{\varLambda}. \tag{3}$$

The generalized Jacobian transformation matrix is given by,

$$\boldsymbol{J}\left(\boldsymbol{\eta}, \boldsymbol{\varOmega}\right) = \begin{bmatrix} \boldsymbol{J}_{1,\boldsymbol{Q}}\left(\boldsymbol{\eta}\right) & 0_{3\times4} \\ 0_{4\times3} & \boldsymbol{J}_{2,\boldsymbol{\varOmega}}\left(\boldsymbol{\varOmega}\right) \end{bmatrix} \tag{4}$$

where

$$\boldsymbol{J}_{1,\boldsymbol{Q}}\left(\boldsymbol{\eta}\right) = \begin{bmatrix} q_0^2 + q_1^2 - q_2^2 - q_3^2 & 2\left(q_1q_2 - q_0q_3\right) & 2\left(q_1q_3 + q_0q_2\right) \\ 2\left(q_1q_2 + q_0q_3\right) & q_0^2 + q_2^2 - q_1^2 - q_3^2 & 2\left(q_2q_3 - q_0q_1\right) \\ 2\left(q_1q_3 - q_0q_2\right) & 2\left(q_2q_3 - q_0q_1\right) & q_0^2 - q_1^2 - q_2^2 + q_3^2 \end{bmatrix}$$

$\boldsymbol{J}_{2,\boldsymbol{\varOmega}}\left(\boldsymbol{\varOmega}\right) = \frac{1}{2}\begin{bmatrix} -\boldsymbol{q}_v^T \\ q_0\boldsymbol{I}_3 - \hat{\boldsymbol{q}}_v^T \end{bmatrix}\boldsymbol{\varOmega}$. $\hat{\cdot}$ denotes the multiplication-cross antisymmetric operator.

The Lagrangian-based uniformized multimodal dynamics for Swift are given,

$$\dot{\boldsymbol{\varLambda}} = \boldsymbol{\varGamma}_1^{-1}\left\{\begin{bmatrix} \boldsymbol{P} \times \boldsymbol{\varOmega} \\ \boldsymbol{\varPi} \times \boldsymbol{\varOmega} + \boldsymbol{P} \times \boldsymbol{V} \end{bmatrix} + m_p\boldsymbol{\varGamma}_3 + \boldsymbol{\tau}_Q\right\} \tag{5}$$

Translational momentum $\boldsymbol{P}$ and angular momentum $\boldsymbol{\varPi}$ are given by

$$\begin{bmatrix} \boldsymbol{P} \\ \boldsymbol{\varPi} \end{bmatrix} = \boldsymbol{\varGamma}_1\begin{bmatrix} \boldsymbol{V} \\ \boldsymbol{\varOmega} \end{bmatrix} + \boldsymbol{\varGamma}_2\dot{\boldsymbol{r}}_p \tag{6}$$

where $\boldsymbol{\varGamma}_1$ and $\boldsymbol{\varGamma}_2$ are defined as,

$$\boldsymbol{\varGamma}_1 = \begin{bmatrix} \boldsymbol{M}_f + m\boldsymbol{I}_3 & -\check{m}\check{\boldsymbol{r}} \\ \check{m}\check{\boldsymbol{r}} & 2\left(\boldsymbol{I}_s + \boldsymbol{I}_p + \boldsymbol{I}_b\right) + \boldsymbol{I}_f \end{bmatrix},$$

$$\boldsymbol{\varGamma}_2 = \begin{bmatrix} m_p\boldsymbol{I}_3 \\ m_p\hat{\boldsymbol{r}}_p \end{bmatrix}, \check{m}\check{\boldsymbol{r}} = m_s\hat{\boldsymbol{r}}_s + m_p\hat{\boldsymbol{r}}_p + m_{b1}\hat{\boldsymbol{r}}_{b1} + m_{b2}\hat{\boldsymbol{r}}_{b2}.$$

The total mass of the vehicle m includes the mass of the fixed structure m_s with the position vector in the BRF $\boldsymbol{r}_s$, the mass of the movable part m_p with the position vector in the BRF $\boldsymbol{r}_p$, the external mass of the hydraulic oil m_{b1} with the position vector in the BRF $\boldsymbol{r}_{b1}$, the inner mass of the oil m_{b2} with the position vector in the BRF $\boldsymbol{r}_{b2}$.

In (5), $\boldsymbol{\tau}_Q$ and $\boldsymbol{\varGamma}_3$ are defined as

$$\boldsymbol{\tau}_Q = \begin{bmatrix} \boldsymbol{J}_{1,\boldsymbol{Q}}^T\left(\boldsymbol{G} + \boldsymbol{B}\right) + \boldsymbol{f}_{ext} \\ \boldsymbol{r}_G \times \left(\boldsymbol{J}_{1,\boldsymbol{Q}}^T\boldsymbol{G}\right) + \boldsymbol{r}_B \times \left(\boldsymbol{J}_{1,\boldsymbol{Q}}^T\boldsymbol{B}\right) + \boldsymbol{\tau}_{ext} \end{bmatrix}$$

$$\boldsymbol{\varGamma}_3 = \begin{bmatrix} -\ddot{\boldsymbol{r}}_p \\ -\hat{\dot{\boldsymbol{r}}}_p\dot{\boldsymbol{r}}_p - \hat{\boldsymbol{r}}_p\ddot{\boldsymbol{r}}_p \end{bmatrix}$$

where $\boldsymbol{f}_{ext}$ and $\boldsymbol{\tau}_{ext}$ denote the environmental force and moment composed of viscous hydrodynamics $\boldsymbol{f}_h(\boldsymbol{\tau}_h)$ and external control forces $\boldsymbol{f}_c(\boldsymbol{T}_c)$, $\boldsymbol{G}$ and $\boldsymbol{B}$ denote the gravity and buoyancy.

(1) (Added) Mass and Inertia: Due to the symmetry of the vehicle [18], the simplified diagonal added mass matrix of Swift can be obtained $\boldsymbol{M}_f = \begin{bmatrix} M_{f1} & M_{f2} & M_{f3} \end{bmatrix}\boldsymbol{I}_3$, the added moment of inertia matrix is $\boldsymbol{I}_f = \begin{bmatrix} I_{f1} & I_{f2} & I_{f3} \end{bmatrix}\boldsymbol{I}_3$. $\boldsymbol{I}_n$ denotes the $n\times n$ unit matrix. The coupling matrix of translation and rotation is denoted as $\boldsymbol{D}_f = \begin{bmatrix} 0 & 0 & 0 \\ 0 & 0 & D_{f1} \\ 0 & D_{f2} & 0 \end{bmatrix}$. The added mass matrix of fixed mass $\boldsymbol{I}_s$, movable mass $\boldsymbol{I}_p$ and oil mass $\boldsymbol{I}_b$ are denoted as $\boldsymbol{I}_s = -m_s\hat{\boldsymbol{r}}_s\hat{\boldsymbol{r}}_s$, $\boldsymbol{I}_p = \boldsymbol{R}_\gamma^T\boldsymbol{I}_{p,0}\boldsymbol{R}_\gamma$, and $\boldsymbol{I}_b = -m_{b1}\hat{\boldsymbol{r}}_{b1}\hat{\boldsymbol{r}}_{b1} - m_{b2}\hat{\boldsymbol{r}}_{b2}\hat{\boldsymbol{r}}_{b2}$ respectively, where $\boldsymbol{R}_\gamma$ denotes the transformation matrix, and $\boldsymbol{I}_{p,0}$ denotes the initial moment of inertia matrix of movable mass,

$$\boldsymbol{R}_\gamma = \begin{bmatrix} 1 & 0 & 0 \\ 0 & \cos\gamma & -\sin\gamma \\ 0 & \sin\gamma & \cos\gamma \end{bmatrix}$$

$$\boldsymbol{I}_{p,0} = \begin{bmatrix} R_p^2 & 0 & -r_{p,x}R_p \\ 0 & r_{p,x}^2 + R_p^2 & 0 \\ -r_{p,x}R_p & 0 & r_{p,x}^2 \end{bmatrix}$$

$\boldsymbol{r}_p = \left[r_{p,x}, r_{p,y}, r_{p,z}\right]^T$ denotes the position vector of movable mass in the BRF. $r_{p,x}$ denotes the displacement along axis $\boldsymbol{e}_0\boldsymbol{e}_1$ in BRF, γ denotes the rotation angle around the axis, R_p denotes the eccentric distance, then the position in BRF can be clearly described by,

$$\boldsymbol{r}_p = \left[r_{p,x}, -R_p\sin\gamma, R_p\cos\gamma\right]^T \tag{7}$$

Since the control signals that manipulate the translational and rotational movements of the movable mass in ARS and the telescopic motion of the piston in BRS are PWM signals driving the DC motor, the response model of the actuators' generalized state $\boldsymbol{\xi} = \left[\boldsymbol{\xi}_1, \boldsymbol{\xi}_2, \boldsymbol{\xi}_3\right]^T$ relative to the control input signal $\boldsymbol{u} = \left[u_1, u_2, u_3\right]^T$ can be expressed based on the simplified motor dynamics,

$$\dot{\boldsymbol{\xi}} = \boldsymbol{\varUpsilon}\boldsymbol{\xi} + \boldsymbol{\kappa}\boldsymbol{u} \tag{8}$$

where $\boldsymbol{\xi}_1 = \left[r_{p,x}, \dot{r}_{p,x}\right]^T$, $\boldsymbol{\xi}_2 = \left[\gamma, \dot{\gamma}\right]^T$, $\boldsymbol{\xi}_3 = \left[r_{b,1}, \dot{r}_{b,1}\right]^T$. $\boldsymbol{\varUpsilon} \in \mathbb{R}^{6\times6}$, $\boldsymbol{\kappa} \in \mathbb{R}^{6\times3}$ are the identified time constant matrix and gain matrix. The detailed model parameters are defined as,

$$\boldsymbol{\Upsilon} = \operatorname{diag}\left\{\boldsymbol{\Upsilon}_1, \boldsymbol{\Upsilon}_2, \boldsymbol{\Upsilon}_3\right\} \tag{9}$$

$$\boldsymbol{\Upsilon}_i = \begin{bmatrix}1 & -\frac{1}{\Upsilon_i}\end{bmatrix}^T \otimes \begin{bmatrix}0 & 1\end{bmatrix} \tag{10}$$

$$\boldsymbol{\kappa} = \operatorname{diag}\left\{\kappa_1, \kappa_2, \kappa_3\right\} \otimes \begin{bmatrix}0 \\ 1\end{bmatrix} \tag{11}$$

where $\otimes$ represents the Kronecker product.

(2) Mass Distribution: Swift is a multi-body system composed of multiple subsystems. The mass distribution is shown in Fig. 1.c. The position vectors corresponding to BRF(IRF) are represented by $\boldsymbol{r}_s(\boldsymbol{q}_s)$, $\boldsymbol{r}_p(\boldsymbol{q}_p)$, $\boldsymbol{r}_{b1}(\boldsymbol{q}_{b1})$, $\boldsymbol{r}_{b2}(\boldsymbol{q}_{b2})$, respectively. Detailed distributions of (displacement) mass are summarized as,

$$\begin{cases} m = m_s + m_p + m_{b1} + m_{b2} \\ \boldsymbol{G} = mg\boldsymbol{k} \\ \boldsymbol{q}_G = \left(m_s\boldsymbol{q}_s + m_p\boldsymbol{q}_p + m_{b1}\boldsymbol{q}_{b1} + m_{b2}\boldsymbol{q}_{b2}\right)/m \\ \boldsymbol{r}_G = \left(m_s\boldsymbol{r}_s + m_p\boldsymbol{r}_p + m_{b1}\boldsymbol{r}_{b1} + m_{b2}\boldsymbol{r}_{b2}\right)/m \end{cases} \tag{12}$$

$$\begin{cases} \varDelta_t = \varDelta_h + \varDelta_b, \varDelta_b = m_{b1}/\rho_2 \\ B_b = \rho_1\varDelta_t, \boldsymbol{B} = -B_b g\boldsymbol{k}, m_0 = m - B_b \\ \boldsymbol{q}_B = \left(\varDelta_h\boldsymbol{q}_h + \varDelta_b\boldsymbol{q}_b\right)/\varDelta_t \\ \boldsymbol{r}_B = \left(\varDelta_h\boldsymbol{r}_h + \varDelta_b\boldsymbol{r}_b\right)/\varDelta_t \end{cases} \tag{13}$$

where $\boldsymbol{k} = [0,0,1]^T$, $g = 9.8m/s^2$ is the acceleration of the gravity, $\varDelta_t$ is the total volume of Swift, $\varDelta_h$ is the volume of the hull, $\varDelta_b$ is the external volume of the oil, $\rho_2 = 850kg/m^3$ is the oil density, B_b is the displacement mass of Swift in seawater of density $\rho_1 = 1021.7kg/m^3$, m_0 denotes the net mass.

(3) Viscous Hydrodynamic Force Analysis: The fluid is assumed to be incompressible and irrotational. Different from the previous hydrodynamic analysis of UG in motion [19], [20], the rotational damping force and moment with zero gliding velocity are specially considered for the attitude transition characterization of Swift in suspension, which are essential for describing the detailed dynamics of dexterous attitude transition. The degree of correspondence between the simulated outcomes and real-world observations is contingent upon the identification precision of the rotational dampling parameters K_p', K_q', and K_r'.

$$\boldsymbol{f}_h = \boldsymbol{R}_3^T \begin{bmatrix} -\left(K_{D0} + K_D\alpha^2\right)\left\|\boldsymbol{V_r}\right\|^2 \\ K_\beta\beta\left\|\boldsymbol{V_r}\right\|^2 \\ -\left(K_{L0} + K_L\alpha\right)\left\|\boldsymbol{V_r}\right\|^2 \end{bmatrix} \tag{14}$$

$$\boldsymbol{\tau}_h = \boldsymbol{R}_3^T \begin{bmatrix} \left(K_{MR}\beta + K_p p\right)\left\|\boldsymbol{V_r}\right\|^2 + K_p' p \\ \left(K_{M0} + K_M\alpha + K_q q\right)\left\|\boldsymbol{V_r}\right\|^2 + K_q' q \\ \left(K_{MY}\beta + K_r r\right)\left\|\boldsymbol{V_r}\right\|^2 + K_r' r \end{bmatrix} \tag{15}$$

where α is the angle of attack, β is the sideslip angle, $\boldsymbol{V_r}$ is the relative water velocity. The values and meanings of other hydrodynamic parameters are shown in Table II.

$$\boldsymbol{R}_3 = \begin{bmatrix} \cos\alpha\cos\beta & -\cos\alpha\sin\beta & -\sin\alpha \\ \sin\beta & \cos\beta & 0 \\ \sin\alpha\cos\beta & -\sin\alpha\sin\beta & \cos\alpha \end{bmatrix}.$$

(4) Control Force and Moment: The control force and moment generated by the vertical rudder and propeller can be expressed as follows,

$$\boldsymbol{f}_c = C_F\rho_1 N^2 D_P^4 \boldsymbol{o}_1 + \frac{1}{2}\rho_1 u^2 S_r \boldsymbol{C}_{RF} \tag{16}$$

$$\boldsymbol{T}_c = C_T\rho_1 N^2 D_P^5 \boldsymbol{o}_1 + \frac{1}{2}\rho_1 u^2 S_r L_r \boldsymbol{C}_{RT} \tag{17}$$

where $\boldsymbol{o}_1 = [1,0,0]^T$, C_F, C_T represent relevant parameters of the thruster, N, D_p, ρ_1 represent the rotate speed, diameter and fluid density of the thruster, respectively. S_r represents the area of the rudder surface, L_r indicates the axial distance of the rudder surface installation position under the BRF. And the vectors of the hydrodynamic coefficient $K_{\delta v}$, $Y_{\delta v}$, and $N_{\delta v}$ related to the rudder angle can be expressed as,

$$\boldsymbol{C}_{RF} = [0, Y_{\delta v}\delta_v, 0]^T \; \boldsymbol{C}_{RT} = [K_{\delta v}\delta_v, 0, N_{\delta v}\delta_v]^T \tag{18}$$

Detailed meanings and values of the parameters refer to Table II.

IV. TRANSITION CHARACTERIZATION AND MOTION ANALYSIS

Experiments are conducted in a pool with a depth of 6m, together with dynamics simulation, to assess the full potential of the dexterous attitude transition and the accuracy of in capturing detailed attitude variation, and to promote the motion performance analysis. The AHRS sensor is installed reasonably according to the setting of BRF, which records the historical attitude response with the sampling frequency of 5Hz. Due to the multi valuedness in the Euler angle output from the AHRS sensor as Swift approaches ±90° in pitch attitude, it is susceptible to abnormal fluctuations in the continuously calculated roll angle readings. To avoid this problem, freezing treatment is used to assist in resolving. The direction cosine $\boldsymbol{C}_b^i$ can be solved online from the data collected by the AHRS sensor as,

$$\begin{aligned} \boldsymbol{C}_b^i &= \begin{bmatrix} c_{11} & c_{12} & c_{13} \\ c_{21} & c_{22} & c_{23} \\ c_{31} & c_{32} & c_{33} \end{bmatrix} \\ &= \begin{bmatrix} \mathrm{c}\theta\mathrm{c}\psi & -\mathrm{c}\phi\mathrm{s}\psi + \mathrm{s}\phi\mathrm{s}\theta\mathrm{c}\psi & \mathrm{s}\phi\mathrm{s}\psi + \mathrm{c}\phi\mathrm{s}\theta\mathrm{c}\psi \\ \mathrm{c}\theta\mathrm{s}\psi & \mathrm{c}\phi\mathrm{c}\psi + \mathrm{s}\phi\mathrm{s}\theta\mathrm{s}\psi & -\mathrm{s}\phi\mathrm{c}\psi + \mathrm{c}\phi\mathrm{s}\theta\mathrm{s}\psi \\ -\mathrm{s}\theta & \mathrm{s}\phi\mathrm{c}\theta & \mathrm{c}\phi\mathrm{c}\theta \end{bmatrix} \end{aligned} \tag{19}$$

where $c(\cdot)$ and $s(\cdot)$ denote $\cos(\cdot)$ and $\sin(\cdot)$ respectively.

When the pitch angle θ is close to -90°, ϕ and ψ satisfy the relationship as,

$$\psi + \phi = \arctan\left(\frac{c_{23} + c_{12}}{c_{13} - c_{22}}\right) \tag{20}$$

When the pitch angle θ is close to +90°, ϕ and ψ satisfy the relationship as,

$$\psi - \phi = \arctan\left(\frac{c_{23} - c_{12}}{c_{13} + c_{22}}\right) \tag{21}$$

Since Swift does not change the heading at the beginning of the transition, the initial mean heading $\psi(t_0)$ can be frozen and substituted into the process (Fig. 6) to calculate $\phi(t_0)$. Alternate freezing of ϕ or θ in the next loop, continually updating until θ is no longer close to ±90°.

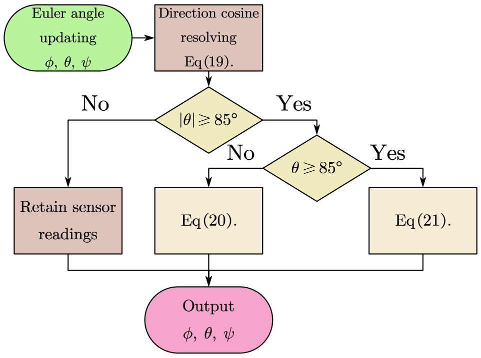

Fig. 6. Flowchart for processing AHRS sensor readings to avoid Euler angle singularity induced abnormal roll angle fluctuations.

A. Drastic Regulation of Pitching Posture

Fig. 7 shows that the actual recorded historical posture response trajectories of Swift with slightly positive buoyancy, during the transition from horizontal to vertical attitude, coincide well with the simulated results. When the nose-down (nose-up) attitude transition is achieved, the corresponding acquired pitch angle is -89°(86°). The pitch angle's adjustment range may be further expanded by the movement of the linear actuator in BRS (refer to Section.4.C). The simulated results can effectively capture the fluctuation of roll response during the transition process. Due to the different setting of the actuator driving speeds, the total actuator adjustment time is 120s (65s), which accounts for 70.6% (60.2%) of the summed transition time (170s for the nose-down transition and 108s for the nose-up transition). By selecting the actuator drive motor with superior performance, the transition time can be further shortened.

There are sluggish matches between the simulated and measured results of ϕ during the period of 120s˜150s in Fig. 7(a) and 60s˜90s in Fig. 7(b). The complex hydrodynamic forces and moments generated by the coupling of the roll and pitch angle affect the accuracy of the simulation in the roll direction at this time. Furthermore, in addition to the form of composition of pitch-direction hydrodynamic parameters, the moment of inertia of the system, which is difficult to estimate accurately, plays a role in influencing the consistency of the simulation results for the pitch angle of 60s˜120s. The enhancement of the accuracy in describing dynamic processes can be achieved through the utilization of well-designed computational fluid dynamics simulations, mechanical modeling with precise configuration of the structural qualities and specific pool experiments.

B. In-situ Heading Maneuvering Adjustment in Cramped Space

Fig. 8 delineates the capacity of Swift's in-situ heading maneuvering adjustment in cramped space, without any assistance of external driver. The heading adjustment results predicted by the model of transition dynamics are consistent with the experimental results, which illustrate that the significant heading adjustment of $\mathit{\Delta}\psi_{actu} = 148^\circ$ ($\mathit{\Delta}\psi_{simu} = 140^\circ$) is achieved in 125s. Elaborated operating sequence of actuators, which controls the translation mechanism first and then rotates at 80s, promotes to achieve the ingenious arrangement of the spatial position of CG. The above operation enables Swift to achieve an intriguing somersault action in the roll direction at 120s. A speedy escape from accidentally entering a confined space is made possible by this in-situ maneuver, which expands the maneuverability of non-externally propelled vehicles.

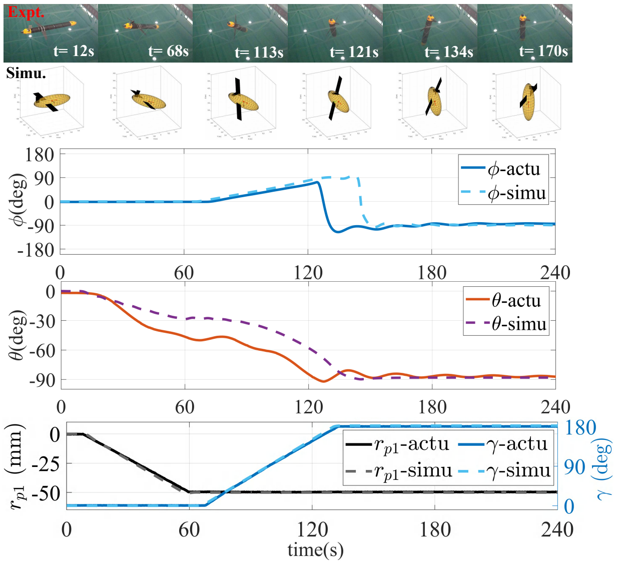

(a) The transition process from horizontal to nose-down attitude.

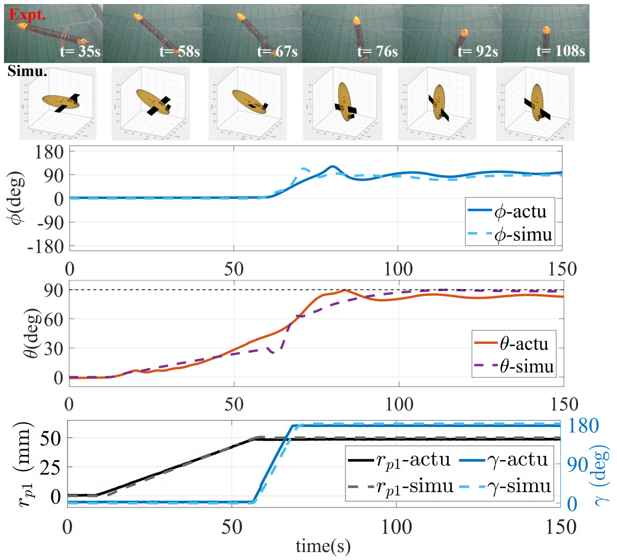

(b) The transition process from horizontal to nose-up attitude.

Fig. 7. Simulated and experimental results of historical attitude and actuator responses during horizontal and vertical attitude transition process of Swift.

C. Vertical Diving and Surfacing Movements

The Swift's motion performance analysis of vertical diving and floating is shown in Fig. 9. Swift adjusts the buoyancy in accordance with the consistency of the heading and the direction of motion thanks to the sensible setup of BRS, which has a clear positive impact on the stability of the vertical pitching. It also proves that reverse excessive regulation will

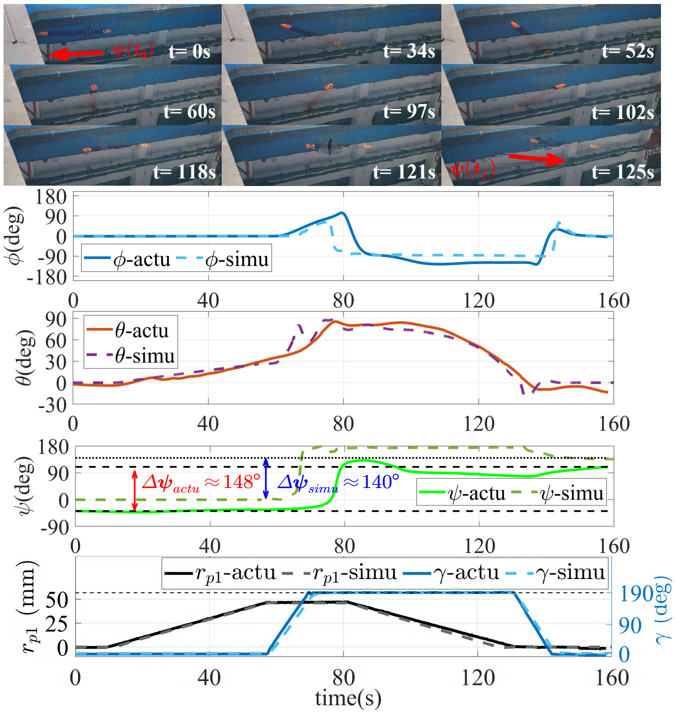

Fig. 8. Simulated and experimental results of historical attitude and actuator responses for in-situ heading maneuvering adjustment.

lead to instability. The pitch angle of Swift can always be maintained at -90°(90°) in the vertical diving (surfacing) state with nose-down (up) attitude. For the scenarios in Fig. 9(a)(120s˜140s) and in Fig. 9(b)(70s˜80s) that are in a loss of vertical posture stabilization, Swift can restore the vertical attitude by simply driving the actuator of the BRS toward the equilibrium or regulating the translation of the ARS to obtain ample metacentric height. As shown in Fig.9(b), during the period of 90s˜130s, Swift has gradually recovered from a vertical destabilized diving ($\theta \approx 60°$) to a vertical floating ($\theta \approx 88°$) to the surface.

D. Transition Between Gliding and Surfacing with Nose-up Attitude

Fig. 10 illustrates the responded dynamics of Swift switching to vertical surfacing with the nose-up attitude from gliding. The actual depth of CG (z-BC) is calculated to represent the real underwater position of Swift by integrating the pitch angle, the characteristic length and the collected data of the stern-installed depth sensor (z-Sen). Swift glides and dives at a pitch angle of -30°, then switches to vertical surfacing with nose-up attitude ($\theta = 88°$) after approaching the bottom of the pool. It should be noted that the transition dynamics-based prediction of the roll and heading responses becomes intractable, due to the bottom collision that occurs at nearly 130s.

V. CONCLUSION

The design overview and experiment-based transition performance analysis for Swift, which is capable of dexterous attitude transition for multiple operation modes, have been presented. The elaborated configuration and the harmonious manipulation of ARS and BRS give Swift the pitch and roll attitude adjustment range of ±90° and the capability of in-situ heading maneuvering adjustment with nearly 150° without any assistance of external driving mechanism. The derived transition dynamics of Swift, which effectually predict the attitude variation, are carried out alongside real experiments to describe the switching characteristics. Experimentally verified attitude stability during vertical diving and surfacing illustrates the effectiveness of the designed layout of BRS. Due to its agile mode switching capabilities, the developed vehicle is compatible with Argo float, UG and AUV. Its synergistic cluster deployment is anticipated to be a new technological revolution for Argo program.

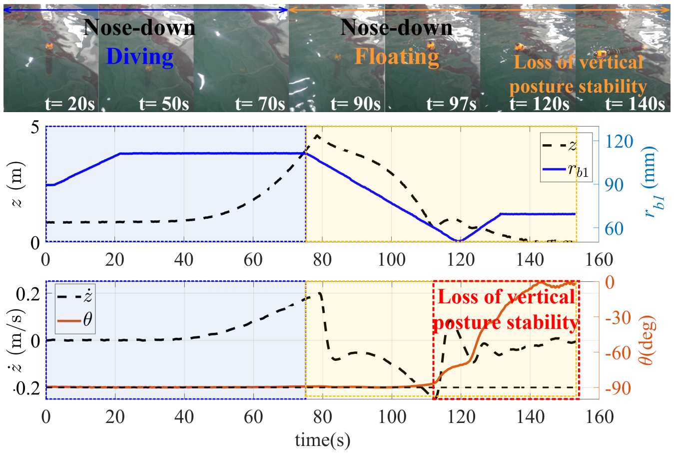

(a) Vertical diving and surfacing with nose-down attitude

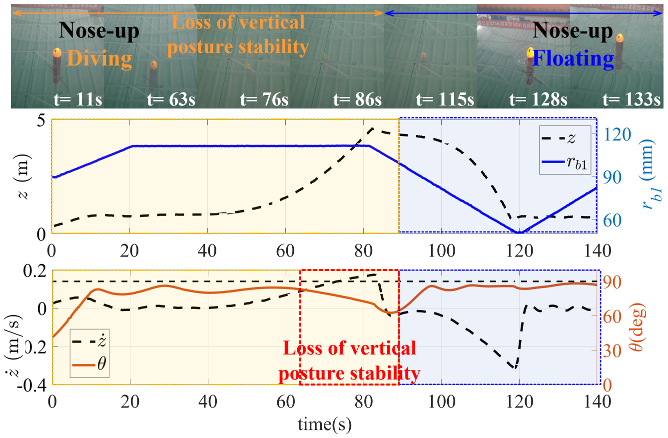

(b) Vertical diving and surfacing with nose-up attitude.

Fig. 9. Experimental results of historical depth, attitude and actuator responses for vertical diving and surfacing.

REFERENCES

[1] A. Brett, J. Leape, M. Abbott, H. Sakaguchi, L. Cao, K. Chand, Y. Golbuu, T. J. Martin, J. Mayorga, and M. S. Myksvoll, "Ocean data need a sea change to help navigate the warming world," *Nature*, vol. 582, no. 7811, pp. 181–183, 2020.

[2] N. V. Sandalyuk, A. Bosse, and T. V. Belonenko, "The 3-d structure of mesoscale eddies in the lofoten basin of the norwegian sea: A composite analysis from altimetry and in situ data," *Journal of Geophysical Research: Oceans*, vol. 125, no. 10, p. e2020JC016331, 2020.

[3] R. Baines, S. K. Patiballa, J. Booth, L. Ramirez, T. Sipple, A. Garcia, F. Fish, and R. Kramer-Bottiglio, "Multi-environment robotic transitions

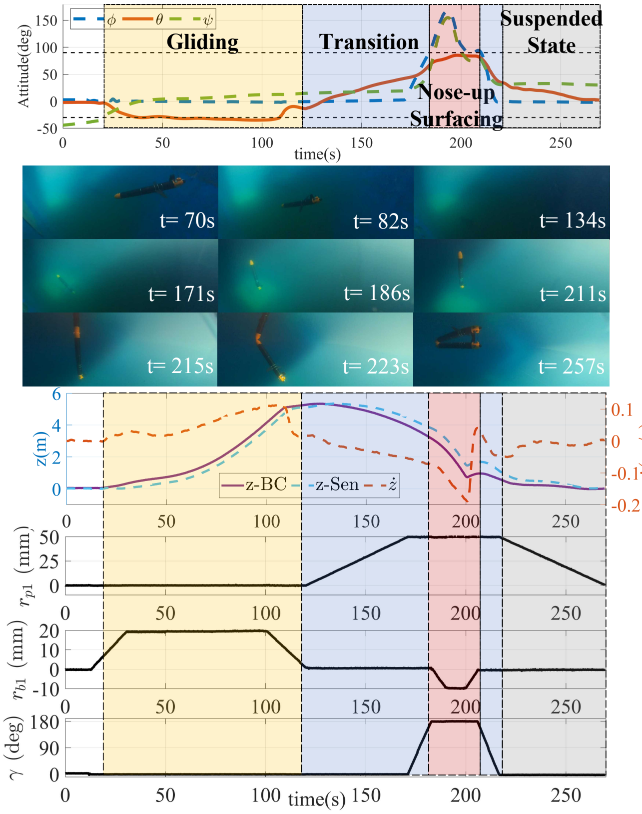

Fig. 10. Experimental results of historical depth, attitude and actuator responses for the transition between gliding and surfacing with nose-up attitude.

through adaptive morphogenesis," *Nature*, vol. 610, no. 7931, pp. 283–289, 2022.

[4] H. Zhou, J. Cao, J. Fu, C. Liu, Z. Wei, C. Yu, Z. Zeng, B. Yao, and L. Lian, "Dynamic modeling and motion control of a novel conceptual multimodal underwater vehicle for autonomous sampling," *Ocean Engineering*, vol. 240, p. 109917, 2021.

[5] C. C. Eriksen, T. J. Osse, R. D. Light, T. Wen, T. W. Lehman, P. L. Sabin, J. W. Ballard, and A. M. Chiodi, "Seaglider: A long-range autonomous underwater vehicle for oceanographic research," *IEEE Journal of oceanic Engineering*, vol. 26, no. 4, pp. 424–436, 2001.

[6] B. R. Page, S. Ziaeefard, A. J. Pinar, and N. Mahmoudian, "Highly maneuverable low-cost underwater glider: Design and development," *IEEE Robotics and Automation Letters*, vol. 2, no. 1, pp. 344–349, 2016.

[7] E. B. Clark, A. Branch, S. Chien, F. Mirza, J. D. Farrara, Y. Chao, D. Fratantoni, D. Aragon, O. Schofield, M. M. Flexas *et al.*, "Station-keeping underwater gliders using a predictive ocean circulation model and applications to swot calibration and validation," *IEEE Journal of Oceanic Engineering*, vol. 45, no. 2, pp. 371–384, 2019.

[8] X. Liao, C. Zhou, Q. Zou, J. Wang, and B. Lu, "Dynamic modeling and performance analysis for a wire-driven elastic robotic fish," *IEEE Robotics and Automation Letters*, vol. 7, no. 4, pp. 11 174–11 181, 2022.

[9] F. Zhang, O. Ennasr, E. Litchman, and X. Tan, "Autonomous sampling of water columns using gliding robotic fish: Algorithms and harmful-algae-sampling experiments," *IEEE Systems Journal*, vol. 10, no. 3, pp. 1271–1281, 2015.

[10] C. Viel, "Self-management of rov umbilical using sliding buoys and stop," *IEEE Robotics and Automation Letters*, vol. 7, no. 3, pp. 8061–8068, 2022.

[11] H. Zhou, J. Cao, B. Yao, and L. Lian, "Hierarchical nmpc–ismc of active heave motion compensation system for tms–rov recovery," *Ocean Engineering*, vol. 239, p. 109834, 2021.

[12] A. Manzanilla, S. Reyes, M. Garcia, D. Mercado, and R. Lozano, "Autonomous navigation for unmanned underwater vehicles: Real-time experiments using computer vision," *IEEE Robotics and Automation Letters*, vol. 4, no. 2, pp. 1351–1356, 2019.

[13] F. Ma, W. Yan, L. Chen, and R. Cui, "Cpg-based motion planning of hybrid underwater hexapod robot for wall climbing and transition," *IEEE Robotics and Automation Letters*, vol. 7, no. 4, pp. 12 299–12 306, 2022.

[14] J. Cao, D. Lu, D. Li, Z. Zeng, B. Yao, and L. Lian, "Smartfloat: A multimodal underwater vehicle combining float and glider capabilities," *IEEE Access*, vol. 7, pp. 77 825–77 838, 2019.

[15] P. Zhou, C. Yang, S. Wu, and Y. Zhu, "Designated area persistent monitoring strategies for hybrid underwater profilers," *IEEE Journal of Oceanic Engineering*, vol. 45, no. 4, pp. 1322–1336, 2019.

[16] P. Wang, X. Wang, Y. Wang, W. Niu, S. Yang, C. Sun, and C. Luo, "Dynamics modeling and analysis of an underwater glider with dual-eccentric attitude regulating mechanism using dual quaternions," *Journal of Marine Science and Engineering*, vol. 11, no. 1, p. 5, 2022.

[17] D. C. Webb, P. J. Simonetti, and C. P. Jones, "Slocum: An underwater glider propelled by environmental energy," *IEEE Journal of oceanic engineering*, vol. 26, no. 4, pp. 447–452, 2001.

[18] N. E. Leonard and J. G. Graver, "Model-based feedback control of autonomous underwater gliders," *IEEE Journal of oceanic engineering*, vol. 26, no. 4, pp. 633–645, 2001.

[19] H. Zhou, J. Fu, C. Liu, Z. Zeng, C. Yu, B. Yao, and L. Lian, "Dynamic modeling and endurance enhancement analysis of deep-sea gliders with a hybrid buoyancy regulating system," *Ocean Engineering*, vol. 217, p. 108146, 2020.

[20] J. Fu, H. Zhou, X. Zhang, H. Wen, B. Yao, and L. Lian, "A unified switching dynamic modeling of multi-mode underwater vehicle," *Ocean Engineering*, vol. 278, p. 114359, 2023.